

## Chirality-Driven Dimensionality and Broadband Emission in Lead Bromide Perovskites

Cássio C. S. Soares <sup>a,b</sup>, Carlos Mera Acosta <sup>a</sup>, Fábio F. Ferreira <sup>a</sup>, Aryane Tofanello <sup>a</sup>, Mayra A. P. Gómez <sup>b</sup>, Alejandro P. Ayala <sup>b</sup>, J. R. Toledo <sup>c</sup>, Yara Galvão Gobato, <sup>c</sup> Maykon A. Lemes <sup>a</sup>, Carlos W. A. Paschoal <sup>b</sup> and José A. Souza\*<sup>a</sup>

<sup>a</sup>Center for Human and Natural Sciences, Federal University of ABC, Brazil, Santo André, Brazil

<sup>b</sup>Department of Physics, Federal University of Ceará, Fortaleza, Brazil

<sup>c</sup>Federal University of São Carlos, Department of Physics, São Carlos, Brazil

**Abstract:** Incorporating chiral organic cations into hybrid organic–inorganic perovskites (HOIPs) offers a unique strategy for tailoring structural dimensionality and modulating photophysical properties. Here, we report that lead bromide perovskites synthesized with chiral ligands R- and S-  $\alpha$ -methylbenzylammonium (MBA) lead to formation of two-dimensional (2D) Ruddlesden–Popper structures while the racemic mixture induces the formation of a hydrated 1D phase,  $(\text{Rac-MBA})_3\text{PbBr}_5 \cdot \text{H}_2\text{O}$ ). DFT calculations show that this transition is driven by electrostatic strain from opposing chiral distortions, which favor octahedral connections with compensated dipoles. Water molecules occupy sites between inorganic chains and mediate hydrogen bonds, stabilizing the 1D motif and relieving strain from racemic reordering. These waters form symmetry-related interstitial networks that mirror the chiral organization, acting as electrostatic compensators in the absence of lateral Pb–Br bonding. Theoretical and experimental characterizations show that the hydrated structure is energetically stable only when four symmetry-related 1D chains and water are present; otherwise, it becomes metallic or unstable. Electronic calculations reveal Rashba-type spin splitting in chiral phases while Br-derived mid-gap states and a Fermi level near the conduction band in the racemic compound. This hydrated phase exhibits pronounced broadband photoluminescence attributed to self-trapped excitons (STEs), and temperature-dependent optical and structural studies reveal that exciton localization and emission dynamics are closely related to octahedral distortions and hydration effects. Our findings demonstrate that stereochemical engineering can offer a robust strategy to modulate dimensionality and optical functionality, with implications for broadband light-emitting applications.

**Keywords:** Halide Perovskites; Chirality; Racemic Cations; Low-Dimensional Materials; Photoluminescence; Self-Trapped Excitons

## 1. Introduction

Hybrid organic–inorganic perovskites (HOIPs) have attracted significant attention due to their exceptional optoelectronic properties and structural tunability, which make them promising candidates for applications in photovoltaics, light-emitting devices, sensors, and photodetectors.<sup>1–4</sup> In particular, low-dimensional lead halide perovskites have emerged as promising materials due to their quantum confinement and dielectric screening effects, enhanced exciton–phonon interactions, and structural versatility afforded by organic spacer engineering.<sup>5–7</sup> One of many strategies to engineer these properties lies in the molecular design of the organic spacer cation, which not only dictates the dimensionality of the perovskite lattice but also modulates electronic structure, exciton dynamics, and lattice stability.<sup>8–11</sup>

The incorporation of chiral organic cations introduces new degrees of freedom in perovskite physics.<sup>12–15</sup> Beyond structural templating, chirality can be transferred from the organic to the inorganic framework, potentially leading to novel optical activity, spin-selective transport, and enhanced light-matter interactions.<sup>16–20</sup> Enantiopure organic cations favor the formation of well-ordered 2D Ruddlesden–Popper structures. At the same time, racemic mixtures can often result in disordered assemblies introducing packing frustration and symmetry breaking, leading to different phases and new photophysical behavior.<sup>21,22</sup> However, the mechanisms by which racemic and enantiopure cations affect the structural dimensionality and enable broadband photoluminescence, particularly through chiral strain and hydration effects, remain to be elucidated.

Here, we present a comparative study of lead bromide perovskites incorporating R-, S-, and racemic  $\alpha$ -methylbenzylammonium (MBA) cations. Our results demonstrate that while enantiopure MBA leads to the formation of highly ordered 2D perovskites, the racemic mixture promotes the formation of an 1D hydrated phase,  $(\text{Rac-MBA})_3\text{PbBr}_5 \cdot \text{H}_2\text{O}$ . This effect is accompanied by the emergence of broad-band self-trapped exciton (STE) emission, in contrast to narrow-band excitonic emission observed in the 2D chiral counterparts. This behavior arises from the combined effects of molecular chirality, packing frustration, exciton–phonon coupling, and structural and electronic responses to hydration. Density functional theory calculations further reveal Rashba-type spin splitting in the chiral phases, and the formation of mid-gap Br-derived states in the 1D racemic structure. These states are stabilized electrostatically by symmetry-related interstitial water molecules, which mediate hydrogen bonding and enforce local dipole

compensation. Structural and temperature-dependent optical studies reveal that racemic distribution and hydration play a key role not only in stabilizing the 1D framework, but also in modulating the bandgap and enabling phonon-assisted recombination. Our results establish a direct link between molecular stereochemistry, dimensional control, and electronic band structure. These findings highlight the role of stereochemical engineering in controlling both the dimensionality and optoelectronic properties of HOIPs, offering new design principles for device based on chiral and racemic molecular components.

## 2. Experimental Section

**Materials:** Lead(II) oxide (PbO,  $\geq$ 99.0%), hydrobromic acid (HBr, 48 wt%), diethyl ether ( $\geq$ 99.9%), (S)-(-)- $\alpha$ -methylbenzylamine (S-MBA, 98%), (R)-(+)- $\alpha$ -methylbenzylamine (R-MBA,  $\geq$ 99.0%), and ( $\pm$ )- $\alpha$ -methylbenzylamine (Rac-MBA, 99.0%) were purchased from Sigma-Aldrich and used without further purifications.

**Synthesis:** In a 25 mL beaker with a magnetic stir bar, 1 mmol of PbO was dissolved in 5 mL of HBr at 120 °C under vigorous stirring for 15 minutes. After dissolution, 2 mmol of S-MBA, R-MBA, and Rac-MBA were added dropwise. The solutions were then stirred for 1 hour before being slowly cooled to room temperature, resulting in colorless microcrystals that were washed several times with diethyl ether to remove any residual solvent and left to dry overnight. Thin films were prepared by dissolving 5 mg of each enantiomer-based perovskite sample in 20  $\mu$ L of DMF, followed by drop-casting the solution onto a quartz substrate at 65 °C for 1 hour.

**Instrumentation:** Powder X-ray diffraction (PXRD) measurements were performed on a STADI-P (Stoe<sup>®</sup>, Darmstadt, Germany) diffractometer operating in Debye-Scherrer geometry. The instrument is equipped with a curved Ge(111) monochromator to select the CuK $\alpha_1$  radiation ( $\lambda = 1.54056$  Å). The powdered sample was loaded into a 0.3 mm diameter glass capillary. Measurements were performed at several discrete temperatures, specifically at 80 K, 100 K, 120 K, 200 K, 330 K, 380 K, 400 K, 380 K, 360 K, 340 K, 320 K, and 300 K, with the temperature being stabilized and controlled by an Oxford Cryostream 1000 series cryostat. Diffraction patterns were recorded in the  $2.000^\circ \leq 2\theta \leq 93.335^\circ$  angular range, with step sizes of  $0.015^\circ$  and an acquisition time of 50 s for each  $1.05^\circ$  scan window. Structural analysis and Rietveld refinements were conducted using the TOPAS-Academic v.7 software.<sup>23</sup> The (R-/S-MBA)<sub>2</sub>PbBr<sub>4</sub> structures were simulated for the refinements from the crystallographic information file of (R-/S-MBA)<sub>2</sub>PbI<sub>4</sub>

(CCDC 607740 and 607741) where the halides were switched for the bromide. The (R-/S-MBA) $\text{PbBr}_3$  (CCDC 1877050 and 1877054) structure was also used in the refinements. Single crystal X-ray diffraction measurements were performed on a Bruker D8 Venture X-ray diffractometer equipped with a Photon II Kappa detector and  $\text{MoK}\alpha_1$  radiation ( $\lambda = 0.71073 \text{ \AA}$ ) microfocus source. The crystal was chosen and mounted on a MiTeGen MicroMount using immersion oil. The APEX 6 software was used for unit cell determination and data collection. The data reduction and global cell refinement were made using the Bruker SAINT<sup>+</sup> software package, and a numerical absorption correction was performed with SADABS.<sup>24,25</sup> The structure was solved by intrinsic phasing method using SHELXT<sup>26</sup> allowing the location of most of the non-hydrogen atoms. The remaining non-hydrogen atoms were located from difference Fourier maps calculated from successive full-matrix least-squares refinement cycles on  $\text{F}^2$  with SHELXL<sup>27</sup> and refined using anisotropic displacement parameters under the graphical interface Olex2.<sup>28</sup> Hydrogen atoms placed according to geometrical criteria and treated using the riding model. Crystallographic data for the structure reported here has been deposited with the Cambridge Crystallographic Data Centre. CCDC 2466728 contain the supplementary crystallographic data for this paper. These data can be obtained free of charge from The Cambridge Crystallographic Data Centre via [www.ccdc.cam.ac.uk/structures](http://www.ccdc.cam.ac.uk/structures). Crystallographic illustrations were obtained using the VESTA software.<sup>29</sup> Scanning electron microscopy analysis was performed in a JSM-6010LA microscope model. Circular dichroism spectra were collected using a JASCO J-815 spectropolarimeter. UV-Visible absorption spectra were evaluated using an Evolution 220 Thermo-Fisher spectrophotometer. Room-temperature photoluminescence measurements were carried out in a Horiba FluoroMax Plus spectrofluorometer. Low temperature optical measurements were performed in a closed-cycle Janis CCS-150 cryostat. A continuous-wave (cw) linearly-polarized CNI laser with a photon energy of 3.88 eV (320 nm) was used to excite the sample. The photoluminescence signal was focused on an Andor Shamrock SR-500i spectrometer coupled with an Andor CCD (iDus DU420A-BU). Differential scanning calorimetry was performed on a Q2000 calorimeter (TA Instruments). The experiment was conducted at a rate of 5 °C/min over a temperature range of 70–180 °C under a nitrogen atmosphere using 5 mg of sample for each run. Raman spectroscopy was performed using a T64000 Jobin Yvon spectrometer equipped with an Olympus microscope and an  $\text{LN}_2$ -cooled CCD to detect the emitted radiation

from the samples in a single mode and a Krypton ion laser operating at a wavelength of 633 nm.

**Density Functional Theory Simulations:** The *ab initio* calculations were performed within the DFT using Perdew–Burke–Ernzenhof (PBE) generalized gradient approximation exchange–correlation functional<sup>30</sup> as implemented in the Vienna *ab initio* simulation package.<sup>31,32</sup> We included the spin–orbit interaction in all calculations to introduce the effect of the noncollinear spin and relativistic corrections with cutoff energies of 500 Ry, k-point sampling of  $6 \times 6 \times 3$  for the experimental atomic configurations at 304 K. The electronic structure has been minimized with a converge criteria of  $10^{-5}$  eV, while the geometry and forces have been set to the experimental configuration without additional atomic relaxation.

### 3. Results and Discussion

Lead bromide-based HOIPs were synthesized using R-/S-/Rac- $\alpha$ -methylbenzylammonium (R-/S-/Rac-MBA) as organic cation spacers. These molecules comprise a secondary carbon bonded to a phenyl, a methyl and a protonated ammonium group, as illustrated in Fig. S1. In order to synthesize  $(R-/S-/Rac-MBA)_2PbBr_4$ , we used the slow evaporation method with an aqueous HBr solution of stoichiometric amounts of PbO and R-/S-/Rac-MBA in a 1:2 ratio as described in the Experimental Section. Fig. 1a,b shows the scanning electron microscopy (SEM) of the obtained samples. The R-/S-MBA based perovskites were in the form of flat needle-like crystals ranging from 50 to 150  $\mu$ m with lamellar conformation. In contrast, the use of the racemic mixture yielded prolonged block-shaped crystals with axes ranging from 50 to 100  $\mu$ m with three well-defined dimensions. Fig. 1c,d shows the room-temperature XRD pattern along with Rietveld refinement of the as-prepared (R-/S-MBA) sample. Both compounds crystallize as mirror images of 2D Ruddlesden-Popper perovskites with orthorhombic crystal structure and Sohncke  $P2_12_12_1$  space group<sup>33,34</sup> revealing inorganic layers of corner-sharing  $PbBr_6$  octahedra in the  $(0\ 0\ 2l)$  planes (where  $l$  is an integer) separated by bilayers of R-/S-MBA cations along the  $c$  axis as shown in Fig. 2a. Weak van der Waals interactions stabilize the organic layers. In contrast, the bonding between the organic and inorganic layers is mediated by hydrogen bonding. The powder XRD also detected a very small amount of the  $(R-/S-MBA)PbBr_3$  1D phase. The experimental PXRD patterns of

$(R/S\text{-MBA})_2\text{PbBr}_4$ , along with the simulated single-crystal XRD patterns of both the 2D phase and the  $(R/S\text{-MBA})\text{PbBr}_3$  phases, are shown in Fig. S2 for comparison.

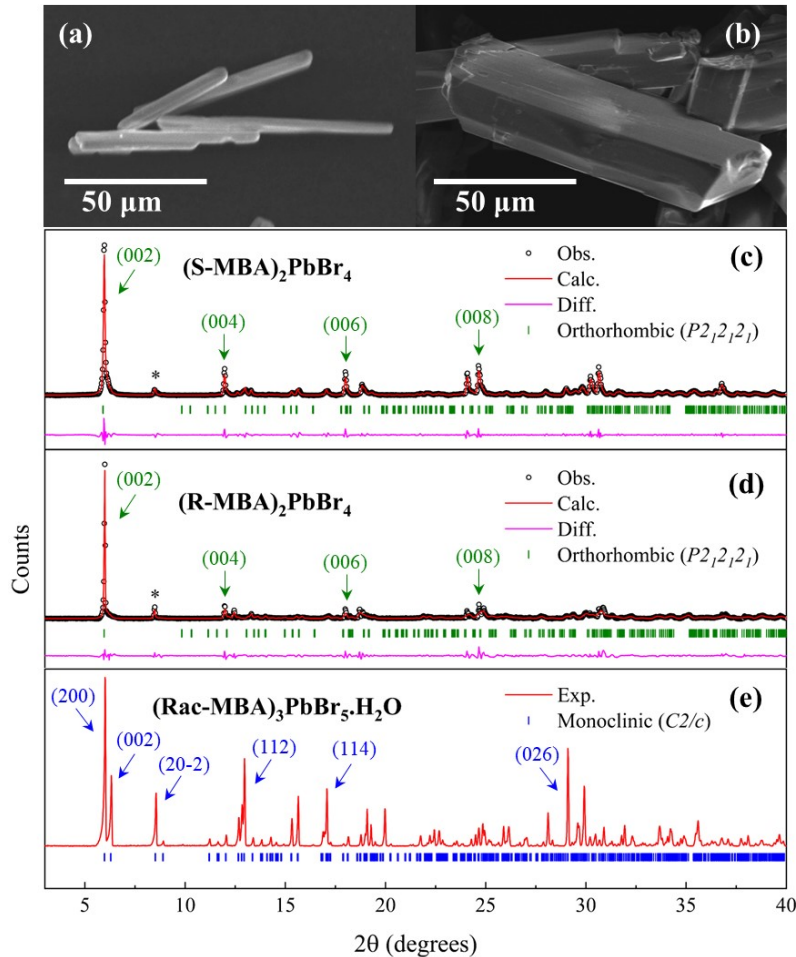


**Fig. 1.** SEM images of the (a)  $(S\text{-MBA})_2\text{PbBr}_4$  and (b)  $(Rac\text{-MBA})_3\text{PbBr}_5\cdot\text{H}_2\text{O}$  microcrystals. Powder XRD data along with Rietveld refinements for the chiral perovskites (c)  $(S\text{-MBA})_2\text{PbBr}_4$  and (d)  $(R\text{-MBA})_2\text{PbBr}_4$ . Tick marks below the XRD pattern indicate the expected Bragg reflection positions considering the orthorhombic phase with  $P2_12_12_1$  space group symmetry for both samples. Asterisks (\*) stands for the (002) plane from traces of  $(R/S\text{-MBA})\text{PbBr}_3$ . (e) Powder XRD and simulated Bragg reflections considering a monoclinic monohydrated 1D  $(Rac\text{-MBA})_3\text{PbBr}_5\cdot\text{H}_2\text{O}$  phase with a  $C2/c$  space group symmetry. Green and blue arrows indicate the most intense diffraction peaks that distinguish the 2D and monohydrated 1D perovskites.

Although the same synthesis procedure was adopted to synthesize 2D perovskites with the racemic mixture in the organic cation site, the Bragg reflections do not belong to the 2D orthorhombic crystal structure as observed for chiral molecules. On the other hand,

single-crystal X-ray diffraction (SCXRD) of the obtained microcrystals revealed the formation of a completely different crystal phase - a monoclinic monohydrated 1D (*Rac*-MBA)<sub>3</sub>PbBr<sub>5</sub>·H<sub>2</sub>O perovskite belonging to the *C2/c* space group that was first reported by Billing and Lemmerer<sup>21,35</sup> as shown in Fig. 1e. This MBA-based perovskite has chains of corner-shared PbBr<sub>6</sub> octahedra running along the *b* axis in a zig-zag pattern. Organic cations surround each chain arranged radially, with their ammonium heads directed toward the chains to form hydrogen bonds with water molecules positioned between adjacent chains, as illustrated in Fig. 2b. Comparative lattice parameters of the (*R*-/S-MBA)<sub>2</sub>PbBr<sub>4</sub> and (*Rac*-MBA)<sub>3</sub>PbBr<sub>5</sub>·H<sub>2</sub>O perovskites are displayed in Table S1 and SCXRD data together with refinement parameters are available in Table S2.

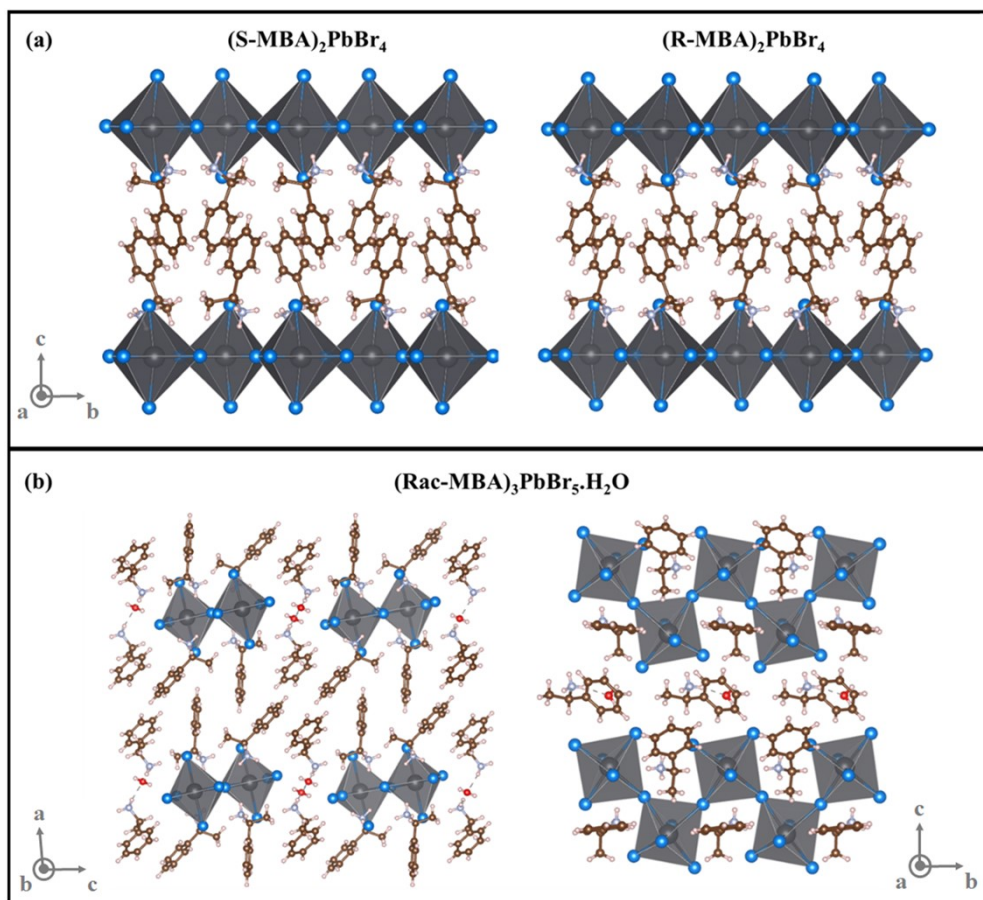


**Fig. 2.** (a) Crystal structures of the 2D perovskites (*S*-MBA)<sub>2</sub>PbBr<sub>4</sub> and (*R*-MBA)<sub>2</sub>PbBr<sub>4</sub>. (b) (left) Schematic representation of the four families of PbBr<sub>6</sub> octahedra formed in the (*Rac*-MBA)<sub>3</sub>PbBr<sub>5</sub>·H<sub>2</sub>O crystal, grouped according to the direction of local polar distortion (dipole) and molecular chirality. These blocks emerge due to opposing lattice strains imposed by alternating R- and S-enantiomers, which inhibit in-plane octahedral

connectivity and promote a one-dimensional chain geometry. (right) 1D arrangement of  $(\text{Rac-MBA})_3\text{PbBr}_5\cdot\text{H}_2\text{O}$ .

Although there are some examples of chiral halide perovskites where structures with different dimensionalities appear upon incorporating racemic cations,<sup>36,37</sup> the underlying mechanism of such phenomena remains not fully defined. The formation of the 1D  $(\text{Rac-MBA})_3\text{PbBr}_5\cdot\text{H}_2\text{O}$  structure, instead of the 2D phases observed for enantiopure  $(\text{R/S-MBA})_2\text{PbBr}_4$  crystals, could be attributed to a combination of electrostatic repulsion and molecular distortions introduced by the racemic mixture. While enantiopure MBA cations adopt a uniform orientation that enables ordered bilayer formation through directional hydrogen bonding and efficient packing, as shown in Fig. 2a, the presence of both R- and S-enantiomers disrupts this supramolecular order. In racemic systems, the coexistence of oppositely handed molecules leads to local dipole cancellation, introducing electrostatic inhomogeneity and long-range Coulombic repulsion between adjacent organic layers. Such electrostatic frustration, coupled with local steric mismatch, can distort the inorganic layers in such a way that inhibit the formation of periodic 2D hydrogen-bonded networks, leading to the reorganization into a lower-dimensional framework of corner-sharing  $\text{PbBr}_6$  octahedra surrounded by radially reorganized MBA cations, as illustrated in Fig. 2b.<sup>38,39</sup>

To investigate the thermal stability of  $(\text{Rac-MBA})_3\text{PbBr}_5\cdot\text{H}_2\text{O}$ , we have performed differential scanning calorimetry (DSC) measurements on the hydrated perovskite in the temperature range of 65–180 °C, as shown in Fig. 3a (red and blue curves correspond to the heating and cooling processes, respectively). In the first heating cycle, a weak endothermic peak is observed beginning around 85 °C, likely associated with residual solution that remained even after cleaning. In addition, another endothermic event is observed starting around 110 °C, which may be associated with the removal of water from the monohydrated 1D perovskite structure as previously reported by Zhou *et al.* through thermogravimetric analysis (TGA).<sup>40</sup> A third endothermic peak appears at 150 °C during heating, followed by an exothermic event at 130 °C during cooling. In the second cycle, performed on the same sample, only the endothermic peak at 150 °C and the exothermic event at 130 °C are present during the heating and cooling processes, respectively, suggesting that an irreversible structural transformation of  $(\text{Rac-MBA})_3\text{PbBr}_5\cdot\text{H}_2\text{O}$  occurred from the release of water. To confirm this phase transformation, we compared the room-temperature XRD patterns of the as-grown

perovskite and the same sample after thermal treatment at 120 °C for 1 hour. As one can see in Fig. 3b, the XRD patterns were markedly different, confirming the irreversible phase transformation indicated by the DSC data. We compared the XRD pattern of the new phase with the precursors as (Rac-MBA)Br and PbBr<sub>2</sub>, as well as the possible 1D and 2D phases of the MBA enantiomers-based perovskites, as shown in Fig. S3, further suggesting a new phase driven by water removal that will be determined elsewhere.

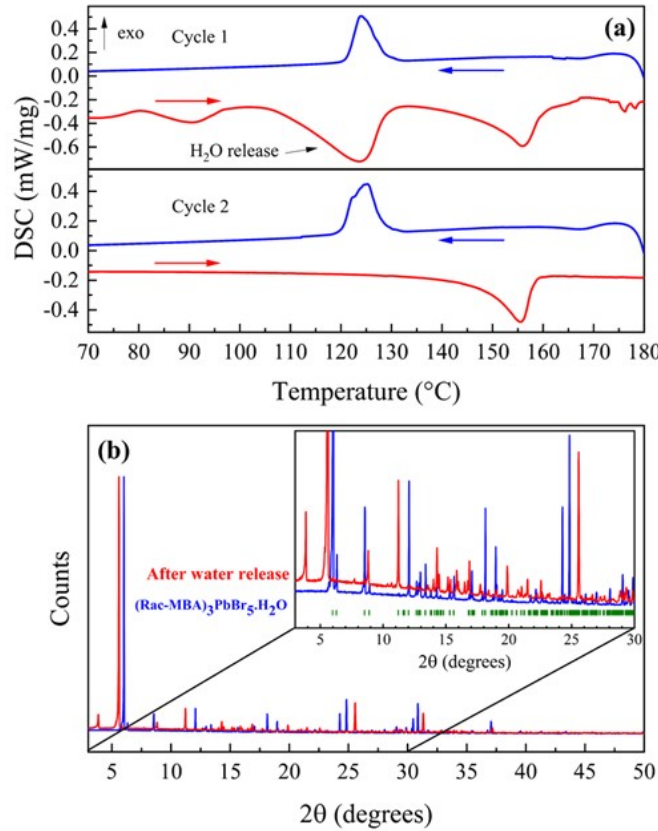


**Fig. 3.** (a) DSC data of  $(\text{Rac-MBA})_3\text{PbBr}_5 \cdot \text{H}_2\text{O}$  performed at the first and second cycles. (b) Powder XRD of the as-grown  $(\text{Rac-MBA})_3\text{PbBr}_5 \cdot \text{H}_2\text{O}$  and the new phase after water release from thermal treatment, both at room-temperature. Green tick marks on the inset represent the expected Bragg reflection positions considering a monoclinic phase with  $\text{C}2/\text{c}$  space group symmetry of the hydrated perovskite.

To understand the influence of molecular chirality and dimensionality on the electronic structure of these materials, we have performed DFT calculations for both the enantiopure and racemic systems. As expected from symmetry considerations, the R- and S-enantiomers yield identical band structures, with no discernible differences in electronic dispersion. The valence band maximum (VBM) primarily comprises of Br *p*-

orbitals in both cases. In contrast, the conduction band minimum (CBM) is dominated by Pb *p*-states, which agrees with previous reports on halide perovskites.<sup>41,42</sup> We corroborate this by *k*-resolved band-character projections, consistent with type-I band-edge ordering on the inorganic Pb–Br network. The calculated bandgap is direct and located at the  $\Gamma$ -point, with a value of approximately 2.8 eV using the PBE functional as shown in Fig. 4a. Although this functional is known to underestimate the absolute bandgap by about 1 eV,<sup>43–45</sup> the relative trends remain reliable. They will be discussed further in the next section. Notably, inclusion of spin–orbit coupling (SOC) reveals a Rashba-like spin splitting at the conduction band minima, with a momentum offset and energy splitting on the order of 10 meV (Fig. 4b), as expected by the chiral-induced deformation in polar materials.<sup>46</sup> Polarization-resolved spectroscopic measurements would be required to isolate the microscopic origin of this splitting and to disentangle SOC-driven effects from possible optical phenomena such as photon recycling or bound excitons emissions.<sup>47,48</sup>

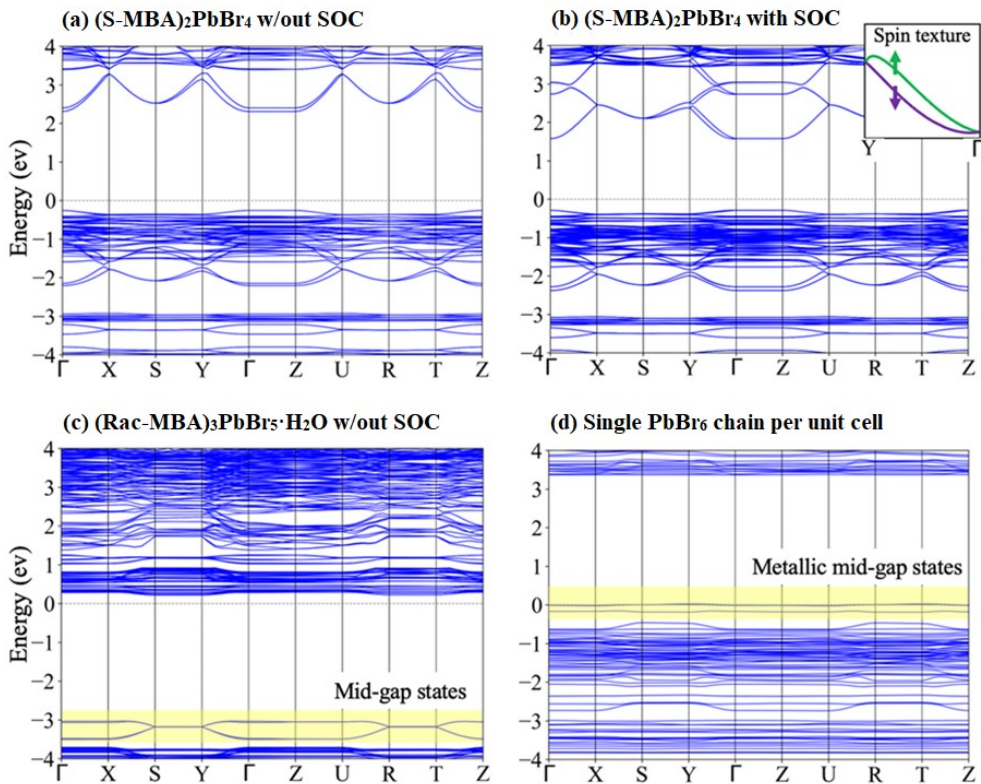


**Fig. 4.** Band structures of enantiopure and racemic lead bromide perovskites. (a) (S-MBA)<sub>2</sub>PbBr<sub>4</sub> without spin–orbit coupling (SOC), showing a direct bandgap at  $\Gamma$ . (b) Same system with SOC, revealing Rashba-type spin splitting at the band edges (~10 meV). The inset shows the spin texture (expectation value of the spin operator), with opposite  $S_z$  orientations depicted in green and purple. (c) (Rac-MBA)<sub>3</sub>PbBr<sub>5</sub>·H<sub>2</sub>O without SOC, showing mid-gap states from undercoordinated Br atoms and a Fermi level near the gap. (d) Single PbBr<sub>6</sub> chain per unit cell, showing metallic mid-gap states.

conduction band. (d) Reduced racemic system with a single  $\text{PbBr}_6$  chain per unit cell, showing metallic behavior due to electrostatic instability.

In contrast, the racemic compound  $(\text{Rac-MBA})_3\text{PbBr}_5 \cdot \text{H}_2\text{O}$  exhibits a significantly reduced bandgap relative to its chiral counterpart. This narrowing originates from mid-gap states derived from Br atoms that lack full coordination due to the disrupted octahedral connectivity in the one-dimensional structure. Although partially stabilized by hydrogen bonding with water molecules, these undercoordinated Br orbitals introduce electronic states deep within the gap region, as revealed in the unfolded band structure (Fig. 4c). Furthermore, the Fermi level lies very close to the conduction band edge, indicating that the hydrated racemic phase behaves as an extrinsic semiconductor—likely a consequence of charge compensation mechanisms facilitated by interstitial water molecules.

To assess the energetic role of the one-dimensional motif, we simulated a configuration where only a single  $\text{PbBr}_6$  chain per unit cell is retained while maintaining water molecules in the lattice. We find that the total energy per atom increases by approximately 3 eV compared to the system containing the four symmetry-related chains with alternating chirality and polarization. This large energy penalty reflects the emergence of electrostatic instability due to the absence of inter-chain dipole compensation. In this reduced symmetry case, the system spontaneously becomes metallic to screen internal fields, a phenomenon reminiscent of surface electrical stabilization in ferroelectric materials<sup>49</sup> (Fig. 4d). Furthermore, we explored the effect of water removal by eliminating interstitial  $\text{H}_2\text{O}$  molecules from the racemic hydrated structure. In all configurations examined, the absence of water leads to a drastic increase in internal energy—by nearly an order of magnitude—indicating that hydration is critical to the structural and electronic stability of the system. These results suggest that upon thermal desorption of water, the material would likely undergo substantial atomic rearrangement to restore electronic balance and minimize electrostatic energy.

Fig. 5a presents the room-temperature UV-Visible absorption spectra of  $(\text{R-}/\text{S-})\text{MBA}_2\text{PbBr}_4$  and  $(\text{Rac-MBA})_3\text{PbBr}_5 \cdot \text{H}_2\text{O}$  crystals. The absorption edges are located at approximately 345 nm for the enantiomer-based compounds, consistent with previously reported absorption spectra of powder samples of these perovskites.<sup>50</sup> For the hydrated 1D phase, the absorption spectrum closely resembles that reported by Dang *et al.*,<sup>21</sup> featuring a small peak centered around 400 nm, which can be attributed to defect-induced

mid-gap states, and a strong peak at 350 nm, commonly assigned to excitonic absorption. The direct bandgap energies were determined via the Tauc plot method to be 3.74 eV and 3.47 eV for the 2D and 1D perovskites, respectively. To confirm whether the incorporation of chiral ligands resulted in chiral perovskites, we performed circular dichroism (CD) spectroscopy on thin films obtained by dissolving the crystals in DMF and spin-coating them onto quartz substrates. This approach was necessary since the as-synthesized crystals were too thick to yield a reasonable CD response. As shown in Fig. 5b, CD signals were observed for  $(R-/S\text{-MBA})_2\text{PbBr}_4$  around 350 nm with oppositely signed values near the absorption edge for each sample, which can be attributed to the Cotton effect.<sup>34,51</sup> This proves that chirality was successfully transferred from the chiral ligands to the inorganic sublattices.

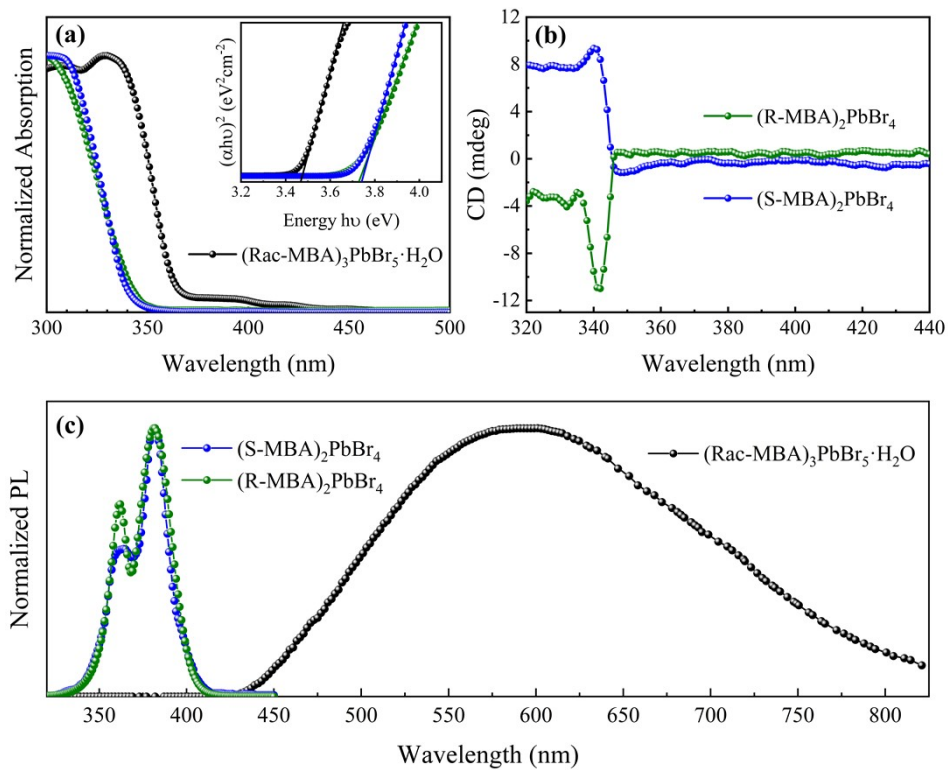


**Fig. 5.** Room-temperature optical properties of the  $(R-/S\text{-MBA})_2\text{PbBr}_4$  and  $(Rac\text{-MBA})_3\text{PbBr}_5\text{·H}_2\text{O}$  perovskites. (a) Normalized absorption spectra with the Tauc plot in the inset. (b) Circular dichroism of the enantiomers-based perovskites. (c) Normalized photoluminescence spectra.

Steady-state photoluminescence (PL) spectra of the samples are shown in Fig. 5c. For the  $(R-/S\text{-MBA})_2\text{PbBr}_4$  compounds, two distinct narrow emissions were detected at 362 nm and 382 nm, both near the absorption edge. The higher-energy PL peak is widely

attributed to free exciton emission in 2D halide perovskites,<sup>52,53</sup> whereas the origin of the lower-energy emission remains under debate. Possible explanations include photon recycling mechanisms, in which a portion of the high-energy emission becomes strongly confined within the crystal, aided by the 2D structural configuration. This confined light can propagate over long distances through total internal reflection, thereby enhancing photon recycling during emission transmission and resulting in a red-shifted subsequent emission, as previously reported for the 2D perovskites  $(BA)_2PbBr_4$  and  $(PEA)_2PbBr_4$ .<sup>48</sup> Another possible mechanism involves spin splitting induced by SOC. Rashba-type splitting has been previously reported as the origin of the double emission feature in the 2D perovskite  $(PEA)_2PbI_4$  and in other 3D hybrid perovskites.<sup>54</sup> As discussed earlier, the inclusion of SOC revealed a Rashba-like spin splitting at the conduction band minimum in  $(S\text{-MBA})_2PbBr_4$ . However, the calculated energy splitting ( $\sim 10$  meV) is significantly smaller than the experimentally observed separation between the double-emission peaks ( $\sim 180$  meV), suggesting that additional mechanisms may also be involved. Nevertheless, the definitive assignment of the PL peaks in the  $(R\text{-}/S\text{-MBA})_2PbBr_4$  compounds would require further experimental analyses, such as power-dependent and time-resolved PL measurements.

An intriguing photoluminescence behavior is observed with the use of the racemic mixture. The  $(Rac\text{-MBA})_3PbBr_5\cdot H_2O$  1D perovskite exhibits a broad-band emission (BE) centered around 600 nm, commonly associated with self-trapped exciton (STE) emission in halide perovskites.<sup>55,56</sup> Similar broad-band emissions are observed in the enantiomer-based 1D perovskites  $(R\text{-}/S\text{-MBA})PbBr_3$ ,<sup>21</sup> although in this case the emission is redshifted compared to the racemic hydrated phase which can be related to the differences in the octahedral connectivity of the  $PbBr_6$  octahedra from corner-sharing type for  $(Rac\text{-MBA})_3PbBr_5\cdot H_2O$  and edge-sharing case  $(R\text{-}/S\text{-MBA})PbBr_3$ . This difference in connectivity can modify the orbital overlap of Pb–Br bonds and alter the conduction/valence bandwidths and effective masses, which in turn can affect how deeply an exciton could be localized in a STE state. The BE indicates STE recombination, facilitated by lattice softness, reduced dimensionality, and hydrated interchain environments. The emergence of STE luminescence in the racemic compound underscores the profound effect of dimensionality and molecular packing on exciton dynamics. Remarkably, an intriguing photophysical behavior emerges with the use of the racemic cations, which results in the formation of a 1D perovskite structure,  $(Rac\text{-MBA})_3PbBr_5\cdot H_2O$ , instead of the 2D phase typically observed with the chiral (R- or S-MBA) analogs. The origin of

this broadband emission can be attributed to a confluence of structural and electronic factors.<sup>57,58</sup> The use of a racemic mixture likely introduces local packing disorder and reduces overall lattice symmetry, which are known to promote lattice deformation and exciton self-trapping. In low-dimensional halide perovskites, such distortions are particularly impactful, as they can localize photoexcited carriers via enhanced exciton–phonon coupling mechanisms.<sup>57,58</sup> Furthermore, the dimensional transition from 2D to 1D significantly enhances exciton–phonon interactions due to reduced dielectric screening and stronger quantum confinement. This effect is further reinforced by interstitial water molecules, which are stabilized between the inorganic chains in the 1D structure. These water molecules can interact dynamically with the organic cations via hydrogen bonding, further softening the lattice and facilitating vibrational modes that support STE formation. The reduced bandgap observed for the 1D Rac-MBA perovskite (3.47 eV) compared to its 2D counterparts (~3.74 eV) also suggests enhanced electronic delocalization along the chain axis, which may aid in the relaxation of excitons into lower-energy self-trapped states.

Temperature-dependent photoluminescence (PL) measurements were performed to investigate the emission behavior of the  $(\text{Rac-MBA})_3\text{PbBr}_5 \cdot \text{H}_2\text{O}$  sample, as shown in Fig. 6a. The BE observed at room temperature blueshifts and rapidly increases its intensity upon cooling until 110 K and reaches saturation around 80–100 K. Below 80 K, the BE redshifts and its intensity decreases followed by the emergence of a narrow-band emission (NE) centered at 410 nm with minor emissions around 350–375 nm that exhibits a relatively large Stokes shift compared to the excitonic peak at 350 nm, but it correlates closely with the absorption feature near 400 nm as shown in Fig. 5a, suggesting that it originates from bound exciton emission associated with mid-gap defect states. The BE profile resembles strong overlapping emission bands as temperature decreases. Although multiple-peak fitting was attempted, the uncertainty in the number of contributing peaks and their irregular shifts with temperature rendered the fitting results unreliable. As we have not observed well resolve bands in the range of the NE emission, we have performed the analysis by considering the entire spectral range of the BE (450–700 nm) and NE (350–450 nm) regions to evaluate the following results.

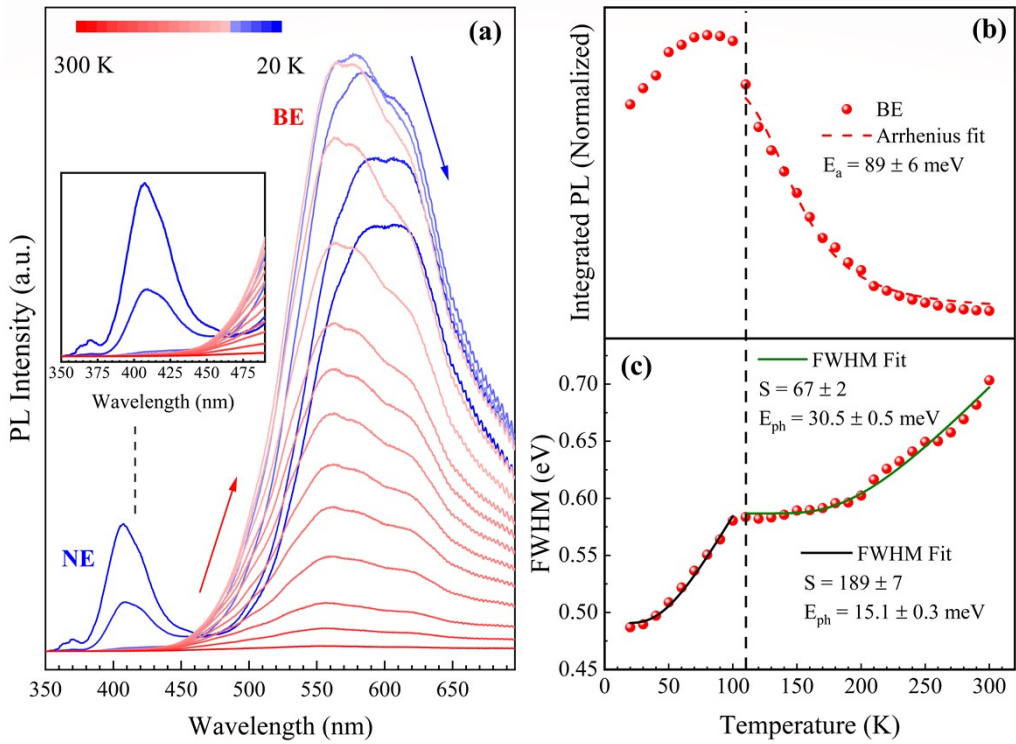


**Fig. 6.** (a) PL temperature-dependence of  $(\text{Rac-MBA})_3\text{PbBr}_5 \cdot \text{H}_2\text{O}$  perovskites. (b) Normalized integrated PL intensity and (c) FWHM of BE dependences on temperature.

The energy barrier that activates nonradiative processes, such as exciton trapping or nonradiative recombination, is referred to as the activation energy  $E_a$  and can be estimated by using the Arrhenius equation<sup>59,60</sup> applied to the integrated PL intensity  $I_{PL}(T)$  dependence on temperature  $T$  according to Equation 1:

$$I_{PL}(T) = \frac{I_0}{1 + Ae^{\frac{-E_a}{k_B T}}} \quad (1)$$

where  $A$  is related to the density of radiative recombination centers,  $I_0$  is the zero-temperature integrated intensity and  $k_B$  refers to the Boltzmann constant. The Equation 1 was applied to the integrated intensity of BE before saturation to obtain its activation energy as shown in Fig. 6b. To estimate  $E_a$  for the NE, because of the weak intensities at temperatures close to 110 K, we performed a linear fit of  $\ln(I_0 I^{-1} - 1)$  as a function of  $(k_B T)^{-1}$  as illustrated in Fig. S4. The results yield  $E_a = 89 \pm 6$  meV for the BE and  $E_a = 9.1 \pm 0.2$  meV for the NE. The activation energy for the BE can be related to the energy barrier for

nonradiative recombination and is consistent with the presence of the broadband even at room temperature (thermal energy  $\sim 25$  meV). Since the emergence of the NE with increasing intensity occurs simultaneously with the reduction of the BE intensity, the low  $E_a$  value for the NE can be interpreted as the energy barrier for exciton trapping.<sup>61</sup> This interpretation is consistent with the appearance of the NE below 110 K (thermal energy  $\sim 9.48$  meV).

As before, the BE is attributed to STEs, which are closely related to the interactions between charge carriers and lattice vibrations. To assess the strength of the exciton–phonon coupling, we analyzed the temperature dependence of the BE linewidth  $\Gamma(T)$ , as shown in Fig. 6c. This dependence can be modeled using Toyozawa’s theory,<sup>62</sup> which employs a configuration coordinate framework where the average number of phonons with an effective energy  $E_{ph}$  emitted during exciton recombination is described by the Huang–Rhys factor  $S$ ,<sup>63</sup> in the form of the Equation 2:

$$\Gamma(T) = \Gamma_0 \sqrt{S} E_{ph} \sqrt{\coth\left(\frac{E_{ph}}{2k_B T}\right)} \quad (2)$$

where  $S \gg 1$  typically indicates strong coupling.<sup>64,65</sup> Analysis of Fig. 6c reveals two distinct regimes above and below 110 K. Shifting the zero-temperature to 110 K, to reflect thermally activated phonons, Toyozawa’s model applied to the PL linewidth data above 110 K yielded  $E_{ph} = 30.5 \pm 0.5$  meV ( $\sim 245$  cm $^{-1}$ ) and  $S = 67 \pm 2$ , which elucidates the strong exciton-phonon coupling usually found in STE emission. In contrast, the analysis below 110 K gives  $E_{ph} = 15.1 \pm 0.3$  meV ( $\sim 122$  cm $^{-1}$ ) and  $S = 189 \pm 7$ . The effective phonon energies could be associated with those seen in the Raman spectrum at 143 cm $^{-1}$  and 230 cm $^{-1}$  as shown in Fig. S5, while the change in phonon energy is expected as higher-energy phonons become frozen out at low temperatures. Notably, the low-temperature Huang–Rhys factor is  $S = 189 \pm 7$  is almost three times higher than the high-temperature value and among the largest reported to date, to the best of our knowledge. The pronounced variation in the Huang–Rhys parameter  $S$  with temperature reflects changes in the effective phonon energy. Since  $S$  represents the average number of phonons emitted during recombination, higher-energy phonons require less phonons to facilitate the same transition, thereby reducing the value of  $S$ .<sup>64</sup>

In order to correlate whether the changes observed in the photoluminescence were related to structural origins, temperature-dependent XRD measurements of (Rac-MBA)<sub>3</sub>PbBr<sub>5</sub>·H<sub>2</sub>O powder were evaluated, as shown in Fig. S6. Rietveld refinement of the diffractograms revealed a continuous decrease of the lattice parameters and unit cell volume from 380 K to 80 K while maintaining its monoclinic crystal structure, as illustrated in Fig. 7a,b (see some selected temperatures in Fig. S7). These results exclude the possibility of structural phase transitions at low temperatures that could modify the electronic structure of the 1D perovskites and prone different emission behavior.

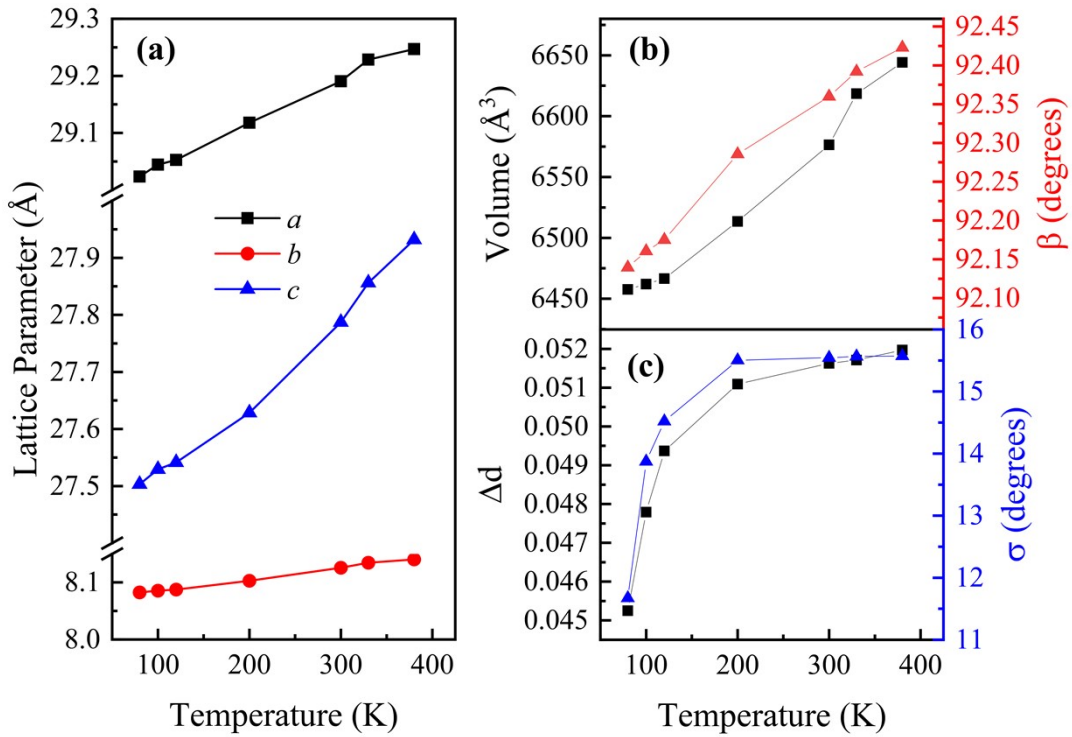


**Fig. 7.** Temperature dependence of the lattice parameters (a) *a*, *b*, *c*, and (b)  $\beta$  along with the unit cell volume of (Rac-MBA)<sub>3</sub>PbBr<sub>5</sub>·H<sub>2</sub>O perovskites. (c) Behavior of octahedra distortions evaluated by the distortion index  $\Delta d$  and bond angle variance  $\sigma^2$  with temperature.

To get insights about the temperature behavior of the inorganic framework, the octahedra distortions were further analyzed through the distortion index

$$\Delta d = \sum_i |d_i - d|/6d$$

, where  $d_i$  is the *i*-th Pb-Br bond length in an octahedron and  $d$  is the

$$\sigma^2 = \sum_i (\theta_i - 90^\circ)^2 / 11$$

average bond length, and the bond angle variance, where  $\theta_i$  represents the  $i$ -th Br-Pb-Br bond angle in an octahedron. As shown in Fig. 7c, the octahedra distortions slowly modify above 120 K, which indicates the persistence of the octahedra configuration. However, the opposite trend is observed in the range of 120 K to 80 K where octahedra distortions decrease with temperature. Octahedral distortions are known to contribute to the formation of self-trapped excitons (STEs), where more distorted environments are prone to exciton trapping.<sup>55,66,67</sup> However, lowering the temperature or applying pressure usually promotes exciton self-trapping by increasing octahedral distortions.<sup>68,69</sup> In contrast, we report an unusual case for (Rac-MBA)<sub>3</sub>PbBr<sub>5</sub>·H<sub>2</sub>O, where lowering temperature reduces octahedral distortions and we propose that these distortions play a central role in governing the photoluminescence behavior of the hydrated 1D phase at low temperatures. Reduced octahedral distortions create a less favorable environment for exciton trapping, enabling the appearance of a high-energy narrow emission alongside the STE band, as not all excitons can be trapped within the more regular octahedral framework. Similar behavior has previously been observed in layered bromide perovskites under pressure.<sup>70</sup>

## Conclusion

In this work, we revealed the influence of molecular chirality on the structural dimensionality and photophysical behavior of lead bromide hybrid perovskites. By systematically comparing enantiopure and racemic  $\alpha$ -methylbenzylammonium (MBA) cations, we demonstrate that subtle changes in molecular stereochemistry can result in different crystallographic and optical properties. Enantiopure MBA cations promote the formation of highly ordered 2D Ruddlesden–Popper perovskites with orthorhombic symmetry, with narrow excitonic emission. In contrast, the racemic MBA mixture induces packing frustration that prevents layered ordering and favors the formation of a 1D hydrated phase (Rac-MBA)<sub>3</sub>PbBr<sub>5</sub>·H<sub>2</sub>O. This dimensional transition is accompanied by the emergence of broadband visible photoluminescence, attributed to the recombination of STEs. Temperature-dependent optical and structural studies reveal that this broadband emission arises from strong exciton–phonon coupling, facilitated by octahedral distortions in the 1D structure. DFT calculations further support these findings

by revealing the emergence of mid-gap states in the racemic structure, arising from undercoordinated Br atoms, and a Fermi level pinned near the conduction band, consistent with extrinsic semiconducting behavior. In the chiral 2D phase, spin-orbit coupling induces Rashba-type spin splitting, highlighting the interplay between chirality and relativistic effects. Energetic comparisons confirm that both interstitial water and the complete set of symmetry-related 1D chains are essential for stabilizing the racemic hydrated phase, with removal of either leading to metallicity or electrostatic destabilization. Our findings establish that racemic mixtures can be strategically exploited to access lower-dimensional frameworks and broadband emitters, expanding the design space for next-generation optoelectronic devices.

### **Acknowledgements**

The authors would like to acknowledge the financial support from Brazilian agencies FAPESP (2021/11446-6, 2024/16896-8, 2023/10982-7, 23/01313-4, 23/11265-7 and 2023/09820-2), CNPq (307778/2023-1, 407956/2022-0, 407954/2022-8, 406322/2022-8, 306827/2023-9, and 310353/2023-8), CAPES (88887.669776/2022-00 and Finance Code 001) and Funcap ((UNI-0210-00047.01.00/23, 07548003/2023). The authors are also grateful for the support from the Experimental Multiuser Center Facilities (UFABC). The authors also acknowledge the financial support from the São Paulo Research Foundation (FAPESP) through the Research, Innovation and Dissemination Center for Molecular Engineering for Advanced Materials - CEMol (Grant CEPID No. 2024/00989-7). The authors also gratefully acknowledge the Multiuser Computational Center at UFABC (CCM-UFABC) for providing the computational resources used in this study.

### **Author contributions**

C. C. S. S. performed the synthesis, SEM, XRD, Raman, UV-Visible absorption, and PL measurements at room-temperature. A. T. performed circular dichroism. J. R. T., and Y. G. G. performed temperature-dependent PL measurements. C. C. S. S. performed temperature dependence PL fit. C. M. A. performed all theoretical calculations. M. A. P. G. and A. P. A. performed the SCXRD measurements and phase determination. F. F. F. performed the temperature-dependent XRD measurements and Rietveld refinements. C. C. S. S. and J. A. S. wrote the manuscript. All the authors contributed to the data analysis

and manuscript revision. J. A. S. supervised the project. After analyzing the results, all authors approved the final version of the manuscript.

### Conflicts of interest

There are no conflicts to declare.

### Data availability

The data that support the findings of this study are available upon request.

### Supplementary information

The online version contains supplementary data such as organic cations representation, XRD patterns, Rietveld refinements, SCXRD data and Raman spectrum.

### References

- 1 J. Fan, W. Li, Q. Zhou, G. Yang, P. Tang, J. He, L. Ma, J. Zhang, J. Xiao, Z. Yan, A. Li and X. Han, *Adv. Funct. Mater.*, 2025, **35**, 2401017.
- 2 H. Dong, C. Ran, W. Gao, M. Li, Y. Xia and W. Huang, *eLight*, 2023, **3**, 3.
- 3 X. Liu, J. Li, X. Cui, X. Wang and D. Yang, *RSC Adv.*, 2022, **12**, 32925–32948.
- 4 E. A. Morais, N. A. M. S. Caturello, M. A. Lemes, H. Ferreira, F. F. Ferreira, J. J. S. Acuña, S. Brochsztajn, G. M. Dalpian and J. A. Souza, *ACS Appl. Mater. Interf.*, 2024, **16**, 4261–4270.
- 5 Q. Zhou, W. Li, J. Xiao, A. Li and X. Han, *Adv. Funct. Mater.*, 2024, **34**, 2402902.
- 6 M. Zhang, L. Zhao, J. Xie, Q. Zhang, X. Wang, N. Yaqoob, Z. Yin, P. Kaghazchi, S. Zhang, H. Li, C. Zhang, L. Wang, L. Zhang, W. Xu and J. Xing, *Nat. Commun.*, 2021, **12**, 4890.
- 7 X. Li, S. Aftab, S. Hussain, F. Kabir, A. M. A. Henaish, A. G. Al-Sehemi, M. R. Pallavolu and G. Kooyada, *J. Mater. Chem. A*, 2024, **12**, 4421–4440.
- 8 P. Gao, A. R. Bin Mohd Yusoff and M. K. Nazeeruddin, *Nat. Commun.*, 2018, **9**, 5028.
- 9 Y. Liu, S. Yuan, H. Zheng, M. Wu, S. Zhang, J. Lan, W. Li and J. Fan, *Adv. Enen. Mater.*, 2023, **13**, 2300188.
- 10 D. Cortecchia, J. Yin, A. Petrozza and C. Soci, *J. Mater. Chem. C*, 2019, **7**, 4956–4969.
- 11 R. I. Sánchez-Alarcón, O. E. Solís, M. C. Momblona-Rincon, T. S. Riolles, J. P. Martínez-Pastor, R. Abargues and P. P. Boix, *J. Mater. Chem. C*, 2024, **12**, 7605–7614.

12 A. Tofanello, A. L. M. Freitas, T. B. de Queiroz, A. Bonadio, H. Martinho and J. A. Souza, *J. Phys. Chem. Lett.*, 2022, **13**, 1406–1415.

13 G. Long, R. Sabatini, M. I. Saidaminov, G. Lakhwani, A. Rasmita, X. Liu, E. H. Sargent and W. Gao, *Nat. Rev. Mater.*, 2020, **5**, 423–439.

14 Y. Dang, X. Liu, B. Cao and X. Tao, *Matter*, 2021, **4**, 794–820.

15 H. Li, R. Cao, M. Tao, J. Jiang and Y. Xiao, *Chem. Sci.*, 2025, **16**, 4057–4065.

16 Z. Ding, Q. Chen, Y. Jiang and M. Yuan, *JACS Au*, 2024, **4**, 1263–1277.

17 M. Moroni, C. Coccia and L. Malavasi, *Chem. Commun.*, 2024, **60**, 9310–9327.

18 J. Son, S. Ma, Y.-K. Jung, J. Tan, G. Jang, H. Lee, C. U. Lee, J. Lee, S. Moon, W. Jeong, A. Walsh and J. Moon, *Nat. Commun.*, 2023, **14**, 3124.

19 J. Ahn, E. Lee, J. Tan, W. Yang, B. Kim and J. Moon, *Mater. Horiz.*, 2017, **4**, 851–856.

20 Y. Asensio, L. Olano-Vegas, S. Mattioni, M. Gobbi, F. Casanova, L. E. Hueso and B. Martín-García, *Mater. Horiz.*, 2025, **12**, 2414–2435.

21 Y. Dang, X. Liu, Y. Sun, J. Song, W. Hu and X. Tao, *J. Phys. Chem. Lett.*, 2020, **11**, 1689–1696.

22 H. Lu, Z. V. Vardeny and M. C. Beard, *Nat. Rev. Chem.*, 2022, **6**, 470–485.

23 A. A. Coelho, *J. Appl. Crystallogr.*, 2018, **51**, 210–218.

24 L. Krause, R. Herbst-Irmer, G. M. Sheldrick and D. Stalke, *J. Appl. Crystallogr.*, 2015, **48**, 3–10.

25 A. L. Spek, *J. Appl. Crystallogr.*, 2003, **36**, 7–13.

26 G. M. Sheldrick, *Acta Crystallogr. A Found. Adv.*, 2015, **71**, 3–8.

27 G. M. Sheldrick, *Acta Crystallogr. C Struct. Chem.*, 2015, **71**, 3–8.

28 O. V. Dolomanov, L. J. Bourhis, R. J. Gildea, J. A. K. Howard and H. Puschmann, *J. Appl. Crystallogr.*, 2009, **42**, 339–341.

29 K. Momma and F. Izumi, *J. Appl. Crystallogr.*, 2011, **44**, 1272–1276.

30 J. P. Perdew, K. Burke and M. Ernzerhof, *Phys. Rev. Lett.*, 1996, **77**, 3865–3868.

31 G. Kresse and J. Furthmüller, *Phys. Rev. B*, 1996, **54**, 11169–11186.

32 G. Kresse and D. Joubert, *Phys. Rev. B*, 1999, **59**, 1758–1775.

33 S. Dan, S. Paramanik and A. J. Pal, *ACS Nano*, 2024, **18**, 35644–35653.

34 L.-S. Yang, E.-C. Lin, Y.-H. Hua, C.-A. Hsu, H.-Z. Chiu, P.-H. Lo and Y.-C. Chao, *ACS Appl. Mater. Interf.*, 2022, **14**, 54090–54100.

35 D. G. Billing and A. Lemmerer, *CrystEngComm*, 2006, **8**, 686–695.

36 A. Abhervé, M. Allain and N. Mercier, *Inorg. Chem.*, 2024, **63**, 5916–5923.

37 M. Li, F. Fang, X. Huang, G. Liu, Z. Lai, Z. Chen, J. Hong, Y. Chen, R. Wei, G.-H. Ning, K. Leng, Y. Shi and B. Tian, *Chem. Mater.*, 2022, **34**, 2955–2962.

38 M. K. Jana, R. Song, H. Liu, D. R. Khanal, S. M. Janke, R. Zhao, C. Liu, Z. Valy Vardeny, V. Blum and D. B. Mitzi, *Nat. Commun.*, 2020, **11**, 4699.

39 S. Maheshwari, M. B. Fridriksson, S. Seal, J. Meyer and F. C. Grozema, *J. Phys. Chem. C*, 2019, **123**, 14652–14661.

40 Y. Zhou, W. Li, X. Chen, X.-Z. Li, X.-J. Wang, B. Bai, Y. Chen and H.-H. Fang, *J. Mater. Chem. C*, 2022, **10**, 15424–15430.

41 S. Tao, I. Schmidt, G. Brocks, J. Jiang, I. Tranca, K. Meerholz and S. Olthof, *Nat. Commun.*, 2019, **10**, 2560.

42 E. Manousakis, *Phys. Rev. B*, 2023, **108**, 045130.

43 W. Kohn, Y. Meir and D. E. Makarov, *Phys. Rev. Lett.*, 1998, **80**, 4153–4156.

44 J. Klimeš, D. R. Bowler and A. Michaelides, *Phys. Rev. B*, 2011, **83**, 195131.

45 T. Björkman, A. Gulans, A. V. Krasheninnikov and R. M. Nieminen, *Phys. Rev. Lett.*, 2012, **108**, 235502.

46 C. Mera Acosta, E. Ogoshi, A. Fazzio, G. M. Dalpian and A. Zunger, *Matter*, 2020, **3**, 145–165.

47 M. C. Gélvez-Rueda, E. M. Hutter, D. H. Cao, N. Renaud, C. C. Stoumpos, J. T. Hupp, T. J. Savenije, M. G. Kanatzidis and F. C. Grozema, *J. Phys. Chem. C*, 2017, **121**, 26566–26574.

48 M. A. Lemes, C. C. Soares, E. A. Morais, Y. J. Onofre, M. P. F. de Godoy, C. W. A. Paschoal, J. J. S. Acuña, C. M. Acosta and J. A. Souza, *ACS Photonics*, 2025, **12**, 3815–3828.

49 K. Garrity, A. M. Kolpak, S. Ismail-Beigi and E. I. Altman, *Adv. Mater.*, 2010, **22**, 2969–2973.

50 C. Zhou, Y. Chu, L. Ma, Y. Zhong, C. Wang, Y. Liu, H. Zhang, B. Wang, X. Feng, X. Yu, X. Zhang, Y. Sun, X. Li and G. Zhao, *Phys. Chem. Chem. Phys.*, 2020, **22**, 17299–17305.

51 J. Ma, C. Fang, C. Chen, L. Jin, J. Wang, S. Wang, J. Tang and D. Li, *ACS Nano*, 2019, **13**, 3659–3665.

52 S. Guo, W. Mihalyi-Koch, Y. Mao, X. Li, K. Bu, H. Hong, M. P. Hautzinger, H. Luo, D. Wang, J. Gu, Y. Zhang, D. Zhang, Q. Hu, Y. Ding, W. Yang, Y. Fu, S. Jin and X. Lü, *Nat. Commun.*, 2024, **15**, 3001.

53 C. Yang, Q. Wei, Y. Gong, M. Long, G. Zhou, G. Xing and B. Wu, *J. Phys. Chem. Lett.*, 2023, **14**, 10046–10053.

54 E. Lafalce, E. Amerling, Z.-G. Yu, P. C. Sercel, L. Whittaker-Brooks and Z. V. Vardeny, *Nat. Commun.*, 2022, **13**, 483.

55 Y. Han, X. Cheng and B.-B. Cui, *Mater. Adv.*, 2023, **4**, 355–373.

56 C. Yang, Q. Wei, Y. Gong, M. Long, G. Zhou, G. Xing and B. Wu, *J. Phys. Chem. Lett.*, 2023, **14**, 10046–10053.

57 Md. Z. Rahaman, S. Ge, C.-H. Lin, Y. Cui and T. Wu, *Small. Struct.*, 2021, **2**, 2000062.

58 A. Biswas, R. Bakthavatsalam, S. R. Shaikh, A. Shinde, A. Lohar, S. Jena, R. G. Gonnade and J. Kundu, *Chem. Mater.*, 2019, **31**, 2253–2257.

59 C. C. S. Soares, J. S. Rodríguez-Hernández, Mayra. A. P. Gómez, D. M. Andrade, P. B. A. Fechine, A. P. Ayala and C. W. A. Paschoal, *J. Mater. Chem. C*, 2024, **12**, 16758–16765.

60 J. Deveikis, M. Giza, D. Walker, J. Liu, C. Wilson, N. P. Gallop, P. Docampo, J. Lloyd-Hughes and R. L. Milot, *J. Phys. Chem. C*, 2024, **128**, 13108–13120.

61 M. D. Smith, A. Jaffe, E. R. Dohner, A. M. Lindenberg and H. I. Karunadasa, *Chem. Sci.*, 2017, **8**, 4497–4504.

62 Y. Toyozawa, *Prog. Theor. Phys.*, 1962, **27**, 89–104.

63 M. de Jong, L. Seijo, A. Meijerink and F. T. Rabouw, *Phys. Chem. Chem. Phys.*, 2015, **17**, 16959–16969.

64 K. M. McCall, C. C. Stoumpos, S. S. Kostina, M. G. Kanatzidis and B. W. Wessels, *Chem. Mater.*, 2017, **29**, 4129–4145.

65 Y. Han, J. Yin, G. Cao, Z. Yin, Y. Dong, R. Chen, Y. Zhang, N. Li, S. Jin, O. F. Mohammed, B.-B. Cui and Q. Chen, *ACS Ener. Lett.*, 2022, **7**, 453–460.

66 X. Wang, W. Meng, W. Liao, J. Wang, R.-G. Xiong and Y. Yan, *J. Phys. Chem. Lett.*, 2019, **10**, 501–506.

67 Z. Ma, F. Li, L. Sui, Y. Shi, R. Fu, K. Yuan, G. Xiao and B. Zou, *Adv. Opt. Mater.*, 2020, **8**, 2000713.

68 L. Zhang, L. Wu, K. Wang and B. Zou, *Adv. Sci.*, 2019, **6**, 1801628.

69 J. Jin, L. N. Quan, M. Gao, C. Chen, P. Guo and P. Yang, *J. Phys. Chem. C*, 2023, **127**, 3523–3531.

70 F.-F. Gao, Y. Qin, Z.-G. Li, W. Li, J. Hao, X. Li, Y. Liu, C. J. Howard, X. Wu, X. Jiang, Z. Lin, P. Lu and X.-H. Bu, *ACS Nano*, 2024, **18**, 3251–3259.